Monthly Notices of the ROYAL ASTRONOMICAL SOCIETY

MNRAS **469,** S774–S786 (2017) doi:10.1093/mnras/stx3008
Advance Access publication 2017 November 23

Dynamics of non-spherical dust in the coma of 67P/Churyumov–Gerasimenko constrained by GIADA and ROSINA data

Stavro L. Ivanovski,[1★] V. Della Corte,[1,2] A. Rotundi,[1,2★] M. Fulle,[3] N. Fougere,[4] A. Bieler,[4] M. Rubin,[5] S. Ivanovska[6] and V. Liuzzi[2]

[1]*INAF - Institute for Space Astrophysics and Planetology, Area Ricerca Tor Vergata, Via Fosso del Cavaliere I-100, Rome 00133, Italy*
[2]*Università degli Studi di Napoli Parthenope, Dip. di Scienze e Tecnologie, CDN I-IC4, Naples 80143, Italy*
[3]*INAF - Osservatorio Astronomico di Trieste, Via Tiepolo I-11, Trieste 34143, Italy*
[4]*Department of Climate and Space Sciences Engineering, University of Michigan, Ann Arbor, MI 48109, USA*
[5]*Physikalisches Institut, University of Bern, CH-3012 Bern, Switzerland*
[6]*Institute of Information and Communication Technologies - Bulgarian Academy of Sciences, 1113 Sofia, Bulgaria*

Accepted 2017 November 21. Received 2017 November 17; in original form 2016 July 9

ABSTRACT

Among the comet 67P/Churyumov–Gerasimenko (67P/C-G) *in situ* measurements, the closest that have ever been performed at a comet nucleus, are also those of speed, mass, and cross-section of cometary grains performed by the Grain Impact Analyser and Dust Accumulator (GIADA) instrument. To interpret GIADA data, we performed dust dynamical numerical simulations with both spherical and non-spherical (spheroids) shapes. This allowed us to analyse how the grain non-sphericity affects the data interpretation. We find that some measured dust speeds are unlikely reproducible when a spherical shape is considered. We considered two GIADA observational periods, 2015 February 19–27 and 2015 March 13–28. Gas parameters calibrated with the Rosetta Orbiter Spectrometer for Ion and Neutral Analysis (ROSINA) measurements have been used to retrieve the gas conditions to set up the dust particle motion. The dust grains are assumed to be out of the near nucleus coma, i.e. where the gas velocity is radial and constant, therefore they are either aligned or have random but constant orientation with respect to the gas drag. We reproduced the GIADA dust speeds, using spheres and two different spheroidal shapes. We find that the particle shapes that reproduce best the GIADA dust speeds are consistent with the particle shape constrained by the GIADA data. We obtain different terminal velocities for spherical and non-spherical particles of the same mass. The shape, which reproduces the GIADA data, is oblate rather than prolate spheroid. We obtain rotational frequencies of the spheroidal particles that best fit the GIADA measurements in these periods.

Key words: methods: numerical – comets: general – comets: individual: 67P/Churyumov-Gerasimenko.

1 INTRODUCTION

The ESA Rosetta mission monitored 67P/C-G at a broad range of heliocentric and cometocentric distances. The collected data opened a room to unravel the driving mechanisms of cometary activity and to answer questions like: which are the dynamical dust properties and the dominant dust cross-sections in dependence on the heliocentric distances and gas coma pattern? Most of the current dust models assumed spherical dust particle (Crifo et al. 2002; Combi, Harris & Smyth 2004; Zakharov et al. 2009; Tenishev, Combi & Rubin 2011). Assuming spherical particles, these models neglect the effect of non-sphericity on particle speed dispersion and disregard how rotational motion could affect the particle dynamics and energy.

While the term *aspherical* is normally used to define small deviations from a perfectly spherical shape when dealing with cosmic dust particles, as in the present work, the *non-spherical* term is adopted. In addition, we refer to ellipsoids of revolution with different aspect ratios as oblate and prolate spheroids.

The motion of non-spherical particles ejected from a spherical homogeneous cometary nucleus has been discussed by Crifo & Rodionov (1999). The authors showed that for randomly spinning convex solids any general relation between the velocity and mass cannot subsist. The velocities reported in Ivanovski et al. (2017) for the group of grains with the same mass and shape also demonstrate different terminal velocities owing to only postulated initial grain

★ E-mail: stavro.ivanovski@iaps.inaf.it (SLI); rotundi@uniparthenope.it (AR)

orientations on the surface and gas production rates. The velocity dispersion of a circular plate with a different thickness-to-radius ratio varies by a factor of 3, provided that the aerodynamical coefficients were calculated for a sphere with the same external area and mass as the plate (Crifo & Rodionov 1999). Ivanovski et al. (2017) varied the aspect ratio of a spheroid from oblate to prolate obtaining a velocity dispersion up to 50 per cent and found that the spherical grain terminal velocity was a lower limit for the oblate shape. The motion of non-spherical grains was obtained computing the active forces at each time-step, integrating over the grains surface. A parallel between the physical conditions of dust motion used by Ivanovski et al. (2017) and by Crifo & Rodionov (1999) should be seen in their limits because of the different assumptions on particle shape and initial orientation. Both groups of authors demonstrated that the aerodynamic force and torque depend on the angle of attack, speed ratio, and assuming no torque at the surface. In addition, Ivanovski et al. (2017) showed the influence of the rotation frequency on particle terminal velocity.

Fulle et al. (2015) used a non-spherical dust model to interpret the data acquired by OSIRIS (Keller et al. 2007) on board Rosetta in the coma of 67P/C-G. They found the best agreement between the computed and the measured rotation frequencies for oblate spheroids.

GIADA measures the physical properties of cometary dust grains by means of three subsystems (Colangeli et al. 2007; Della Corte et al. 2014): the Grain Detection System (GDS) (Epifani et al. 2002), the Impact Sensor (IS) (Esposito et al. 2002), and the Micro Balance System (MBS) (Palomba et al. 2002). GDS optically detects a grain crossing a laser curtain (100 cm^2 large and 3 mm thick) and measures its scattered light. The IS is a *0.5-mm-thick* aluminium square diaphragm (100 cm^2 sensitive area) equipped with five piezoelectric sensors (PZTs), the output of which is monotonically related to the momentum of the impacting grain. When the grain is detected by GDS a time counter switches on and it stops when IS detects the grain impact. By means of the time-of-flight, the speed of the grain is measured. The coupled GDS+IS system (a field of view of 37°) measures speed, time-of-flight, momentum, and mass of each of the detected particle.

In this paper, to check the consistency between the computed dynamical parameters and GIADA measurements, we used a dust dynamical model [described in details in Ivanovski et al. (2017)] considering both spherical and non-spherical particles. We used 3D+t gas solutions calibrated by ROSINA data (Fougere et al. 2016).

Dust particle trajectories are governed by different forces present in the cometary coma. The dominant active forces in the circumnuclear coma are the aerodynamic force and gravity. We computed these forces using the following Rosetta results: mass of the nucleus (Pätzold et al. 2016), gas dynamics constrained by ROSINA data (Fougere et al. 2016), and the dust mass and cross-section measured by GIADA (this work).

Our non-spherical model provides complementary information for particles detected by GIADA, e.g. rotational properties consistent with OSIRIS results on rotating 67P/C-G dust grains (Fulle et al. 2015). The model can compute 3D+t motion of rotating grains considering the aerodynamic and gravitational torque and rotation along any of the particle axis. The model can reproduce dust particle speeds measured by GIADA throughout the Rosetta mission (Della Corte et al. 2015, 2016b). Cometary dust grains are not spherical and a realistic model needs to incorporate the impact of non-sphericity on the dust motion. In the present work, we utilized the coupled GDS+IS GIADA dust detections that provided individual particle mass and speed. In addition, we used the particle geometrical cross-sections that are derived by applying calibration curves (Della Corte et al. 2016a) obtained on cometary analogues (Rotundi et al. 2002; Ferrari et al. 2014) to GDS optical cross-section measurements. We computed the dust speeds of spherical and non-spherical particles with the same masses and cross-sections as those measured by GIADA. The model was used to reproduce the GIADA dust speeds and density of individual particles assuming shapes consistent with those constrained by GIADA [fig. 1 of Fulle et al. (2016, 2017)]. Our simulations allowed us to investigate the impact of non-sphericity on dust particle dynamics having GIADA data as ground-truth.

2 NON-SPHERICAL DUST MODEL

We present an analysis of GIADA data using our numerical 3D+t non-spherical dust model, which for the current purpose traces the motion of single dust particle in the 67/C-G coma. Besides the effects of the active forces governing the dust motion, i.e. the aerodynamic and gravity, the model takes into account the torque that particles strongly experience due to their non-sphericity. The numerical implementation considers that the flow over the particle is in free molecular regime and we take advantage of the expressions of pressure and shear stress (Shen 2006) acting on the particles to compute the aerodynamic force.

We neglect particle collisions and the effect of the solar radiation pressure because it is not the dominant force close to the comet nucleus (within 5 nucleus radii), whereas the gas drag, coupled with the dust in the circumnuclear coma, reacts on short time-scales and is thus the dominant force. Our simulations show that the solar radiation pressure force could become the main force affecting the motion at distances of about 5.5 nucleus radii, when particles have already reached their terminal velocities. We do not consider the effects of dust particle charging because the dust charge plays a role for sizes less than one micron and the estimated particle sizes constrained by GIADA data are much bigger.

2.1 Mathematical formulation of non-spherical dust motion

We use the formulation of the centre of mass motion of homogeneous and convex bodies (axial symmetric spheroids with different aspect ratios) (for details see Fulle et al. 2015; Ivanovski et al. 2017):

$$m_d \frac{\mathrm{d}^2 \boldsymbol{r}}{\mathrm{d}t^2} = m_d \frac{\mathrm{d}\boldsymbol{v}_d}{\mathrm{d}t} = \boldsymbol{F}_N + \boldsymbol{F}_\mathrm{a}, \tag{1}$$

where $\boldsymbol{r}$ and $\boldsymbol{v}_d$ are the radius-vector and the velocity of the centre of mass in the fixed cometocentic frame x, y, z; m_d is the grain's mass and the active forces are the gravity $\boldsymbol{F}_N$ and the aerodynamic force $\boldsymbol{F}_\mathrm{a}$. The angular momentum relative to the centre of mass $\boldsymbol{K}_c$ is:

$$\boldsymbol{K}_c = \int (\boldsymbol{l} \times \boldsymbol{v}) \mathrm{d}m = I\boldsymbol{\omega}, \tag{2}$$

where $\boldsymbol{l}$ and $\boldsymbol{v} = \boldsymbol{\omega} \times \boldsymbol{l}$ are the radius-vector and the velocity of elementary volume of the grain with the mass dm, $\boldsymbol{\omega}$ is a vector of instantaneous angular velocity, and I is a tensor of inertia. From the law of variation of the angular momentum we obtain in the moving frame (i.e. attached to the grain, with origin at the grain centre of inertia and axes along the principal moment of inertia, I_{xx}, I_{yy}, I_{zz}) the Euler dynamical equations:

$$\begin{aligned} I_{xx}\dot{\omega}_x + (I_{zz} - I_{yy})\omega_y\omega_z &= M_x, \\ I_{yy}\dot{\omega}_y + (I_{xx} - I_{zz})\omega_z\omega_x &= M_y, \\ I_{zz}\dot{\omega}_z + (I_{yy} - I_{xx})\omega_x\omega_y &= M_z, \end{aligned} \tag{3}$$

where $\boldsymbol{M}$ is the moment of momentum of external forces.

Equations (1) and (3), and kinematic Euler equations (for details see Landau & Lifshitz 1969), provide the system of differential equations that describes the motion of a grain.

The nucleus gravity force and torque are expressed as

$$\begin{aligned} \boldsymbol{F}_N &= -\int G\tfrac{m_N m_d}{r^3}\boldsymbol{r}\,\mathrm{d}\Gamma \\ \boldsymbol{M}_N &= -\int G m_N \tilde{\rho}\int \tfrac{\boldsymbol{l}_s\times\boldsymbol{r}}{r^3}\mathrm{d}\Gamma \end{aligned} \tag{4}$$

and the aerodynamic force and torque are:

$$\begin{aligned} \boldsymbol{F}_\mathrm{a} &= -\int \left(p\boldsymbol{n} + \tau\left[(\boldsymbol{V}_r\times\boldsymbol{n})\times\boldsymbol{n}\right]/|V_r|\right)\mathrm{d}s, \\ \boldsymbol{M}_\mathrm{a} &= -\int \boldsymbol{l}_s\times\left(p\boldsymbol{n} + \tau\left[(\boldsymbol{V}_r\times\boldsymbol{n})\times\boldsymbol{n}\right]/|V_r|\right)\mathrm{d}s. \end{aligned} \tag{5}$$

Here, p, τ are the gas pressure and the shear stress of the elementary surface element with area ds, $\boldsymbol{n}$ is the outward unit vector normal to the element, G is the gravitational constant, $d\Gamma$ is the elementary volume of the body, and $\boldsymbol{l}_s$ is the radius-vector to the elements ds or $d\Gamma$ from the centre of mass.

From our estimations we conclude that the role of the gravitational torque in the dust motion is negligible under the considered cometary conditions. At close distances (up to a few tens nucleus radii, i.e. the acceleration region) to the comet $\boldsymbol{M}_\mathrm{a}$ is found to be always dominant (Ivanovski et al. 2017).

In order to use the free molecular expression for the calculation of the aerodynamic force and to have the numerical integration correct, the following conditions have to be fulfilled:

(i) the minimal mean-free path of the gas molecules in a spherically expanding flow has to be much higher than the considered dust grains sizes, i.e. providing free molecular regime;

(ii) the reflected molecules must leave the grain's circumscribed sphere in much less than a period of grain's rotation, i.e. $\frac{2\pi}{\omega} \gg \frac{1}{4}l_\mathrm{r}\sqrt{\frac{\pi m}{8k_b T_d}}$ where l_r is the radius of the particle's circumscribed sphere, ω and T_d are the particle's angular velocity and temperature, m is the molecule mass and k_B is the Boltzmann constant (Ivanovski et al. 2017).

(iii) the process of gas flow over the particle must not be stochastic, i.e. the collisional frequency must be much greater than the rotational frequency.

For the 67P/C-G coma conditions discussed in this paper (see Section 3.3), the ratio between the minimal mean-free path of the molecules versus the size of the particles is much greater than 10. The flow over the particle can be considered uniform at each time-step because the flow gradients are larger than the particle size. Then the classical free molecular expressions for gas pressure and shear stress (Shen 2006) could be applied for the aerodynamic forces acting on each elementary surface element of the moving particle.

We assumed that the grains were homogeneous and did not change their shape and mass during the motion. This implies that the particles did not contain any volatile material nor did they fragment. The particles were assumed to be isothermal and maintain constant temperature during their motion. Therefore, we constrained the properties of the impacting molecules reflection which in turn had influence on the aerodynamic force and torque, i.e. the gas molecules reaching the grain were scattered back diffusely with full accommodation of momentum and energy. We assumed that initially the dust grain was placed at the nucleus surface and was at rest. We choose the initial grain orientation with respect to the gas flow direction (i.e. the angle of attack is between the long axis of the dust grain and the local outflow direction). We investigate the motion of convex spheroidal dust grains with the velocity vector always in the plane of rotation, and the direction of the rotational vector always constant.

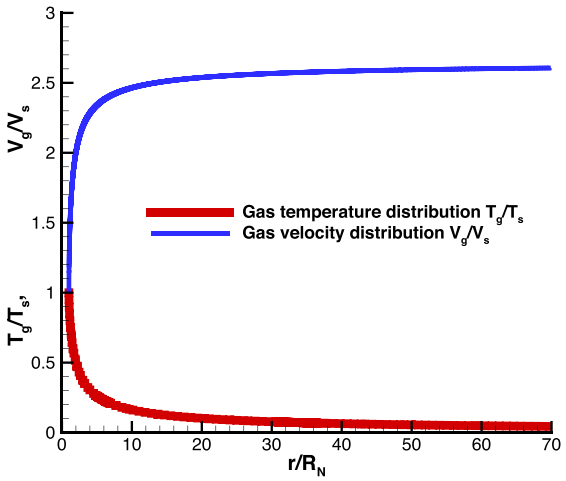

Figure 1. Radial distribution of gas temperature and velocity T/T_s, v/v_s.

The mass and the principal moments of inertia for a spheroid are:

$$m_d = \frac{4}{3}\pi a b^2 \tilde{\rho} \tag{6}$$

$$I_{zz} = \frac{2}{5}m_d b^2;\; I_{xx} = I_{yy} = \frac{1}{5}m_d(a^2+b^2), \tag{7}$$

where $\tilde{\rho}$ is the dust grain bulk density [kg/m^3] and z is the axis of revolution of the spheroid, a is the size of the semi-axis along z, and b is the size of the other two semi-axes.

2.2 Model gas outflow

To describe the gas field we recalled the classical well-known dimensionless analytical functions for the gas velocity, temperature (reproduced here on Fig. 1), and density at any distance r (for details see Gombosi 1994). These are dependencies for the gas parameters of a homogeneous, non-rotating spherical nucleus with a given radius R_N and uniform surface temperature T_s. We assumed the nucleus was emitting both H_2O and CO_2 molecules at a constant production rate Q_g. In the observational period we considered H_2O was the dominant gas species. The initial mass density of the flow was $\rho_s = Q_\mathrm{g} m/(4\pi R_\mathrm{N}^2 V_\mathrm{s})$ assuming an ideal gas expanding into vacuum with initial temperature T_s and corresponding sonic velocity $V_\mathrm{s} = \sqrt{\gamma T_\mathrm{s} k_\mathrm{B}/m}$ where γ is the gas specific heat ratio, k_B is the Boltzmann constant, and m is the mass of the molecule m.

In order to minimize computational time, in our model, we used a simplified gas coma approximation, i.e. the expanding gas flow approximation, which is valid only if the gas coma flow is radial and homogeneous. To verify the feasibility of our approach, i.e. that in the coma region that we aimed to simulate subsisted the radial and homogenous flow, we performed calibrations of Euler gas solutions for expanding flow using the realistic 3D+t simulated gas computations (see Section 3.4) obtained by Fougere et al. (2016) applying a Direct Simulation Monte Carlo model with the Adaptive Mesh Particle Simulator code (Tenishev, Combi & Davidsson 2008; Tenishev et al. 2011; Fougere 2014). We applied our calibration in sectorial patterns of the realistic 3D+t simulated coma (Fougere et al. 2016) small enough to hold the radial and homogeneous flow regime.

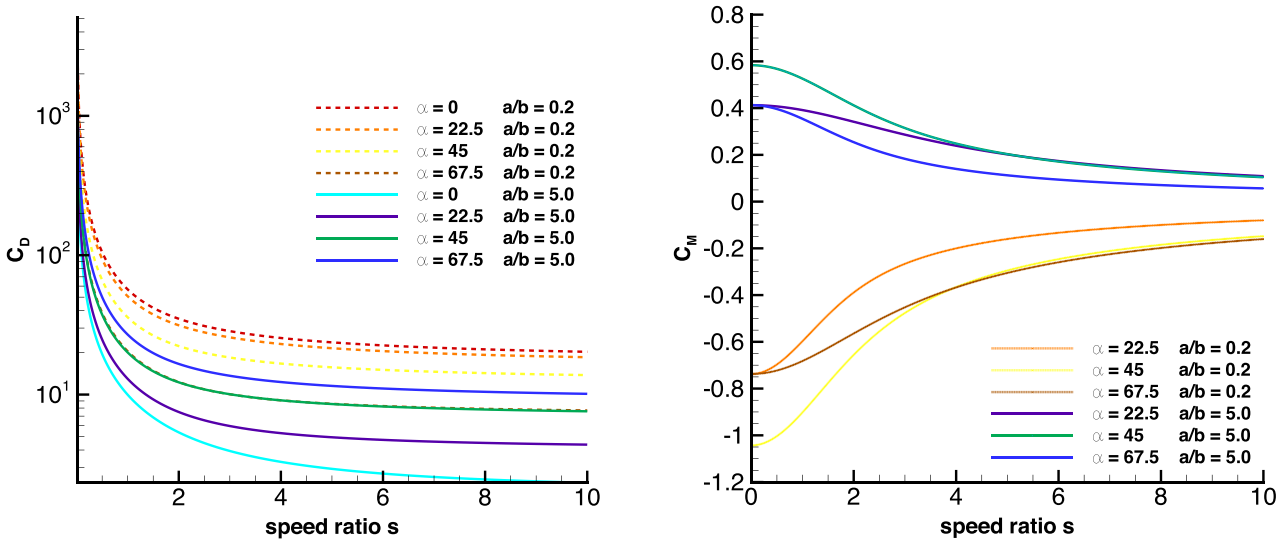

Figure 2. Drag coefficient (left) and torque coefficient (right) as functions of the molecular speed ratios $s = V_r\sqrt{m/(2k_BT_g)}$ for given angle of attack α for spheroids of the same volume with $a/b = 0.2$; 5.0 with $T_d/T_g = 5$.

2.3 Aerodynamic force and torque under free-molecular conditions

The aerodynamic force and torque can be represented by the dimensionless aerodynamic coefficients. Ivanovski et al. (2017) introduced the drag aerodynamic coefficient C_D and the dimensionless aerodynamic torque coefficient C_M as follows:

$$C_D = \frac{\boldsymbol{D}}{1/2\rho V_r^2 S};\ C_M = \frac{\boldsymbol{M}_a}{1/2\rho V_r^2 SA}, \tag{8}$$

where $\boldsymbol{D}$ is the drag force, $\boldsymbol{V}_r = \boldsymbol{V}_g - \boldsymbol{V}_d$ is the gas–grain (centre of mass) relative velocity vector, ρ is the gas mass density, $(\rho V_r^2/2)$ is the dynamic pressure, A is a shape-dependent characteristic linear dimension of the grain, and S is a shape-dependent characteristic cross-section.

Integrating equations (4) and (5) over the grain surface using the free molecular expressions for p and τ (Shen 2006) we have computed the coefficients C_D, C_M as a function of molecular speed ratios $s = V_r\sqrt{m/(2k_BT_g)}$ for several angle of attacks α (angle between the axis of rotation of the ellipsoid and the vector V_r). We have chosen a temperature ratio $T_d/T_g = 5$ and characteristic cross-section, πb^2. As it was done in Ivanovski et al. (2017),the drag coefficients of the oblate grain (a/b=0.2) were multiplied by $(\kappa^{\rm prolate}/\kappa^{\rm oblate})^{2/3}$ (where $\kappa = a/b$). This was done to ensure that the obtained C_D values correspond to forces acting on grains of same volume, hence of same mass, provided that grains have the same bulk density. Fig. 2 shows a strong variation in C_D and C_M for the different initial grain orientations. C_D for the oblate grains (a/b= 0.2) are higher for smaller angles of attack and higher than the corresponding drag coefficient for the prolate grains (a/b= 5.0). For example, for $s = 6$ for α= 0°, C_D values for the oblate grains are 10 times higher than the prolate ones, while for α= 67.5 their values are similar. For small s, C_M for the oblate shape is two times greater than C_M for the prolate shape. A different initial grain orientation leads to variations in the grain motion, testified by the strong variation of the aerodynamic coefficients (Fig. 2).

3 GIADA DATA, MODEL SETUP, AND GAS FLOW CALIBRATION

3.1 Rosetta observational periods

We consider two Rosetta observational periods: 2015 February 19–27 (hereafter P1) and 2015 March 13–28 (hereafter P2). Both periods are characterized by high rates of GIADA detections (GDS+IS) providing speed, geometrical cross-section, and mass of individual compact particles (Della Corte et al. 2016b), good candidates to be studied as convex bodies. In the two selected periods, Rosetta performed five fly-bys with different closest approach distances from the nucleus. Fig. 3 shows Rosetta trajectory in the body-fixed reference frame (Preusker et al. 2015, Cheops reference frame). The fly-bys at low phase angles, small distances, and over high northern latitudes resulted to be an optimal observational scenario for GIADA and for dust coma characterization: high dust detection rates allowed Della Corte et al. (2016b) to assess the dust spatial distribution and to track the particle velocity variations with respect to particle mass. During P1, Rosetta flew down to 55 km (closest approach in February) and back to 110 km from the 67P/C-G nucleus; in P2 during the fly-bys Rosetta reached four different closest approaches: at 70 km (on March 16), 80 km (on March 19), 80 km (on March 22), and 50 km (on March 27).

3.2 GIADA measurements

GIADA measurements of mass, speed, and geometrical cross-section of individual particles during P1 and P2 periods are reported in Table 1. The average speed during P1 is 6.43 m s^{-1} and during P2 is 7.68 m s^{-1}, corrected for the spacecraft relative motion. The error of the GIADA speed measurements is less than 6 per cent (Rotundi et al. 2015). 70 per cent of the detected particles have masses in the range 10^{-8} to 10^{-7} kg.

Fig. 4 shows compact particle masses versus geometrical cross-sections measured by GIADA during P1 and P2 periods. The data are encompassed by the theoretical trends of prolate spheroids (upper lines) with aspect ratio 10 and 5 and bulk density 4600 kg m^{-3} (Fe-sulphides), and oblate ones (lower lines) with aspect ratio 1/10

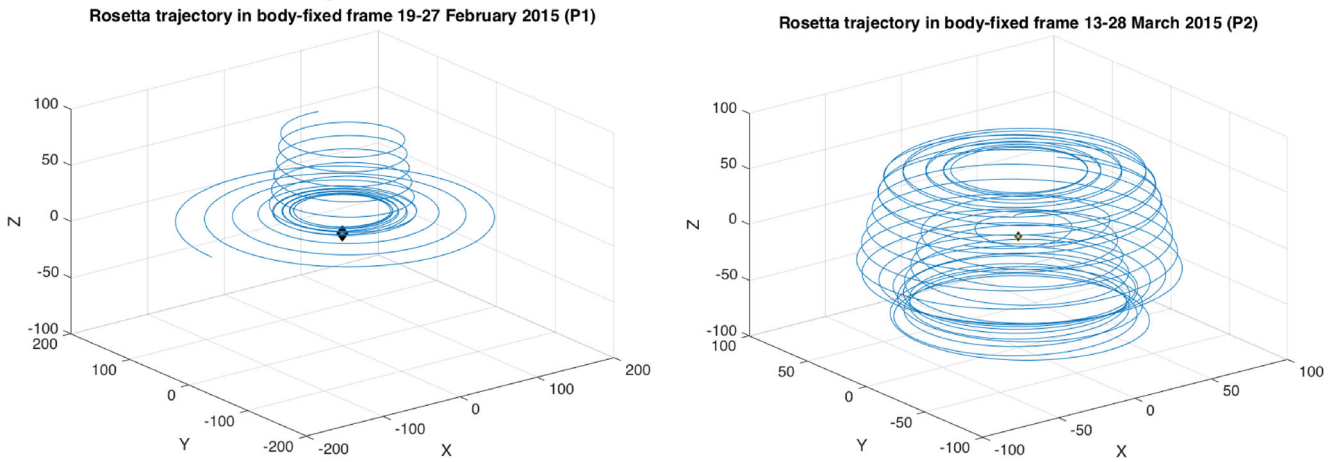

Figure 3. Rosetta's trajectory around 67P/C-G nucleus during the observational periods P1 (2015 February 19–27) (left) and P2 (2015 March 13–28) (right) in body-fixed reference frame. The nucleus centre is at the origin of the axes.

Table 1. GIADA measurements of dust particle speeds, masses, and cross-sections during 2015 February 19–27 (observational period P1) and 2015 March 13–28 (observational period P2). The error of the GIADA speed measurements is less than 6 per cent (Rotundi et al. 2015).

Event day	Event hour	Particle speed [m s^{-1}]	Particle mass m_d [kg]	Particle cross-section [μm^2]
19/02/15	6:33 AM	4.39	1.76E-08 ± 4.01E-09	3.12E+04 ± 2.60E+03
20/02/15	10:57 AM	7.04	3.14E-08 ± 6.28E-09	8.92E+04 ± 7.82E+03
22/02/15	8:23 AM	5.48	1.88E-08 ± 7.82E-09	7.55E+05 ± 8.41E+04
23/02/15	2:04 PM	7.45	2.39E-08 ± 5.05E-09	4.66E+04 ± 2.93E+03
23/02/15	4:58 PM	7.55	2.94E-08 ± 6.20E-09	1.19E+05 ± 1.12E+04
23/02/15	7:37 PM	5.70	4.39E-08 ± 1.13E-08	2.32E+05 ± 2.42E+04
24/02/15	6:31 AM	6.85	3.58E-08 ± 9.37E-09	2.98E+05 ± 3.18E+04
24/02/15	7:02 AM	5.14	8.70E-08 ± 1.07E-08	4.01E+05 ± 4.36E+04
26/02/15	8:49 AM	8.13	6.97E-08 ± 1.83E-08	6.50E+05 ± 7.20E+04
26/02/15	7:50 PM	7.65	3.88E-08 ± 1.74E-08	4.00E+04 ± 2.18E+03
27/02/15	10:52 PM	5.40	5.10E-08 ± 1.21E-08	5.29E+04 ± 3.66E+03
13/03/15	9:25 PM	0.34	1.69E-07 ± 4.97E-08	3.78E+04 ± 4.30E+03
14/03/15	7:56 AM	4.82	4.71E-08 ± 6.93E-09	3.06E+04 ±1.10E+03
14/03/15	10:06 AM	3.20	7.28E-08 ± 2.66E-08	4.61E+05 ± 5.05E+04
14/03/15	7:56 PM	8.91	3.38E-08 ± 1.05E-08	4.64E+04 ± 2.91E+03
15/03/15	9:23 AM	10.42	1.62E-08 ± 6.11E-09	3.43E+04 ± 3.41E+03
15/03/15	12:27 PM	6.04	5.52E-08 ± 1.91E-08	5.53E+04 ± 3.93E+03
15/03/15	5:06 PM	10.54	4.44E-08 ± 8.90E-09	7.69E+04 ± 1.43E+04
15/03/15	5:22 PM	12.33	1.11E-08 ± 3.26E-09	7.05E+05 ± 7.84E+04
15/03/15	9:56 PM	13.39	3.29E-08 ± 6.59E-09	6.52E+04 ± 5.07E+03
16/03/15	1:08 AM	16.89	1.81E-08 ± 7.39E-09	6.48E+04 ± 1.12E+04
16/03/15	1:37 AM	9.77	1.06E-08 ± 3.73E-09	7.27E+04 ± 1.32E+04
16/03/15	7:14 AM	7.36	4.04E-08 ± 8.97E-09	4.94E+04 ± 3.25E+03
16/03/15	12:20 PM	7.24	2.45E-08 ± 6.02E-09	8.88E+04 ± 7.77E+03
16/03/15	11:43 PM	10.72	1.56E-08 ± 3.68E-09	1.00E+05 ± 9.05E+03
18/03/15	5:22 AM	7.47	3.44E-08 ± 7.45E-09	6.52E+04 ± 5.07E+03
22/03/15	7:39 AM	5.80	8.26E-09 ± 3.09E-09	1.48E+05 ± 1.45E+04
26/03/15	7:07 PM	5.13	3.23E-08 ± 8.97E-09	8.12E+04 ± 6.89E+03
28/03/15	9:04 AM	4.73	4.28E-08 ± 1.50E-08	1.04E+05 ± 9.50E+03
28/03/15	10:54 AM	0.41	3.38E-07 ± 9.72E-08	4.83E+04 ± 3.12E+03

and 1/5 and bulk density 1200 kg m^{-3} (hydrocarbons). The selected aspect ratios and the dust bulk density range are determined by GIADA measurements (Fulle et al. 2016, 2017). The comparison between GIADA data and these theoretical trends allowed us to constrain the aspect ratio of the particles detected by GIADA during P1 and P2, assuming they are spheroids. We favoured spheroids because: (1) Rosetta data provide evidence that 67P/C-G dust particles are elongated and rotate (Fulle et al. 2015; Langevin et al. 2016); (2) spheroids are the first step forward in improving the unrealistic spherical assumption; (3) spheroids, having different moments of inertia along different axes, when rotating, exhibit different aerodynamical behaviour with respect to spheres. We used spheroids (and spheres) with masses and cross-sections as measured by GIADA. The sizes of the spheroids are calculated starting from the

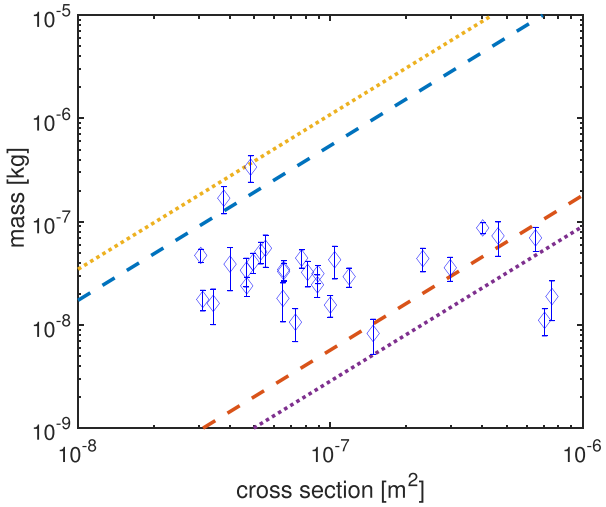

Figure 4. Dust mass and cross-section of particles detected by GIADA in periods P1 (2015 February 19–27) and P2 (2015 March 13–28). The GIADA data are compared with trends of prolate spheroids of aspect ratio of 10 and 5 and with bulk densities 4600 kg m^{-3} (upper lines) and oblate spheroids of aspect ratio 1/5 and 1/10, with bulk density 1200 kg m^{-3} (lower lines), respectively. The errors of the measured cross-sections are not reported here, as being less than 30 per cent the effect on the dust dynamical simulations resulted to be negligible.

cross-section measurements and assuming four limiting cases for the orientation of the particles when entering GIADA (Fig. 6). We checked which particle elongation and orientation reproduced best the GIADA measured dust speeds. The obtained dust terminal velocities are compared with the measured GIADA particle speeds and are discussed in Section 4.

3.3 Non-spherical dust model setup

Our non-spherical dust simulations have a number of input parameters reported in Table 2. These parameters are grouped in four sets with respect to their physical meaning. The first group deals with the physical properties of the dust particles. They are either taken from the GIADA measurements (i.e. particles masses and cross-sections) or calculated assuming the orientation of the detected particle when entering GIADA, choosing a deduced shape constrained by the GIADA data. The second group refers to the initial Euler gas flow parameters that describe the gas coma calibrated with 3D+t DSMC gas solutions (see Section 3.5). The third group is dedicated to the measured physical parameters of the 67P/C-G, necessary to compute the gravity force in the model. The last group includes the specific time-step parameters used in the simulations, in particular, the time-step in each simulation is constrained by the necessary conditions for rarefied gas field approach as reported in Ivanovski et al. (2017).

3.4 Simulated gas coma constrained by ROSINA measurements

In order to compute the gas drag force acting on the dust grains, 3D+t gas dynamical solutions of the coma evolution are necessary. Here, we took advantage of the 3D DSMC gas coma modelling discussed in detail in Fougere et al. (2016). Fig. 5 shows the time-dependent 3D gas solutions for 2015 February 24 and 2015 March 16, representative examples for each of the two periods, P1 and P2, respectively. These gas solutions were constrained by *in situ* ROSINA measurements. It is important to note that in the solutions the gas coma becomes homogeneous at about 30 km from the nucleus and most of the GIADA detections in P1 and P2 are at distances three times farther. The gas flow is not only homogenous but also radial, as shown by the gas velocity streamlines (Fig. 5, bottom right). This allows us to approximate the 3D+t solutions with analytical spherical gas expansion, provided that each analytical solution is consistent locally with the 3D+t gas solution. We note that computing the coupled dust motion with the 3D+t gas coma solutions demands extensive computational time and tuning for the gas coma boundary conditions. As P1 and P2 GIADA detections occurred out of the near nucleus coma, i.e. $>5R_N$, we keep the gas flow solutions rather simple.

3.5 Calibration of the gas flow solutions

To use the Euler gas solution we need to first calibrate the 3D+t gas coma parameters so that the two different gas approximations overlap along the particle's trajectory. The calibration consists in comparing the gas density and velocity obtained with the Euler solutions with those calculated with the 3D+t solutions at different distances from the nucleus. To compute the Euler solution of ideal gas expanding into vacuum these input parameters are necessary: the gas specific heat ratio γ, the mass of the molecule m, the radius of the nucleus R_N, the surface temperature T_s, and the gas production rate Q_g. Taking into account the abundances of the main gas coma agents, H_2O and CO_2, and the listed parameters, with a feedback process we finally obtained gas velocities and densities as those obtained via 3D+t gas numerical simulations.

The adjustment of the gas analytical solutions with respect to the 3D+t gas solutions was performed in two steps: (1) evaluation of the abundances of H_2O and CO_2 and (2) estimation of the total gas production rate for the observational periods P1 and P2 based on the simulated DSMC gas outputs for the number density and gas speed. The H_2O and CO_2 coma abundances were strongly correlated with the nucleus surface activity distribution, due to the complex shape of the comet, and solar illumination. Several studies of the ROSINA (Balsiger et al. 2007) and VIRTIS (Coradini et al. 2007) instruments show evidence for a strong variation of the relative abundances of the different volatiles (Fougere et al. 2016). The authors reported values in terms of CO_2/H_2O production rates of 3 to 10 per cent along the comet's orbit. For the total production rate ratios of $Q(CO_2)/Q(H_2O)$ we found: 6 per cent for 2015 February 24 at 00:00 UT and 4 per cent for 2015 March 16 at 00:00 UT, respectively. Fink et al. (2016) analysed VIRTIS-M imaging spectrometer data and obtained 5 per cent for 2015 February 28 and total water gas production rate of 2.5×10^{26} mol s^{-1}.

We estimated the total gas production rate for the two periods P1 and P2 adopting conservation of mass at constant velocity, i.e. $Q_g = 4\,\pi\,r^2\,v_g\,n_g$, where n_g is the gas number density and r is the distance from the comet nucleus. We scaled this gas production rate with respect to H_2O and CO_2 abundances.

4 RESULTS

In this article, we computed the dynamical properties of every single grain detected by GIADA in P1 and P2 observational periods. Each computation is a trajectory simulation of an individual grain that has the physical properties as measured (or constrained) by GIADA. Therefore, in our computations we do not perform any statistical

Table 2. The model initial parameters.

Input parameter	Parameter value	Comments
	Particle parameters	
Particle mass [kg]	$8.3 \times 10^{-9} - 3.4 \times 10^{-7}$	Measured by GIADA
Particle size [m]	$5.0 \times 10^{-5} - 2.0 \times 10^{-4}$	Constrained by the GIADA cross-section measurements (this work)
Spheroid aspect ratio, a/b	0.1, 0.2, 5, 10	Compatible with the GIADA measurements (Fulle et al. 2016, 2017)
Initial particle orientation [deg]	$0^\circ - 90^\circ$	The range covers all possible particle orientations
Particle temperature, T_d [K]:	200	Assumed to be equal to the averaged value of the nucleus surface (Capaccioni et al. 2015)
	Initial gas field parameters	
Speed [m s^{-1}]	350–500	Derived by the Euler gas flow solutions calibrated with the DCMC 3D+t gas solutions (this work) constrained by ROSINA data (Fougere et al. 2016).
Gas composition	$H_2O + CO_2$	
Gas stream temperature [K]	$10^{26} - 10^{28}$	
Total gas production [mol/s]	100	
Gas stream density [kg/m^3]	5.0×10^{-6}	
	67P/C-G parameters	
Radius, R_N [m]	2.0×10^3	Sierks et al. (2015)
Mass, m_N [kg]	1.0×10^{13}	Pätzold et al. (2016)
Surface temperature, T_N [K]	200	Capaccioni et al. (2015)
	Simulation parameters	
Time-step	0.001	
Number of time-steps	3.0×10^7	Necessary conditions to fulfil the rarefied gas field approach (Ivanovski et al. 2017).

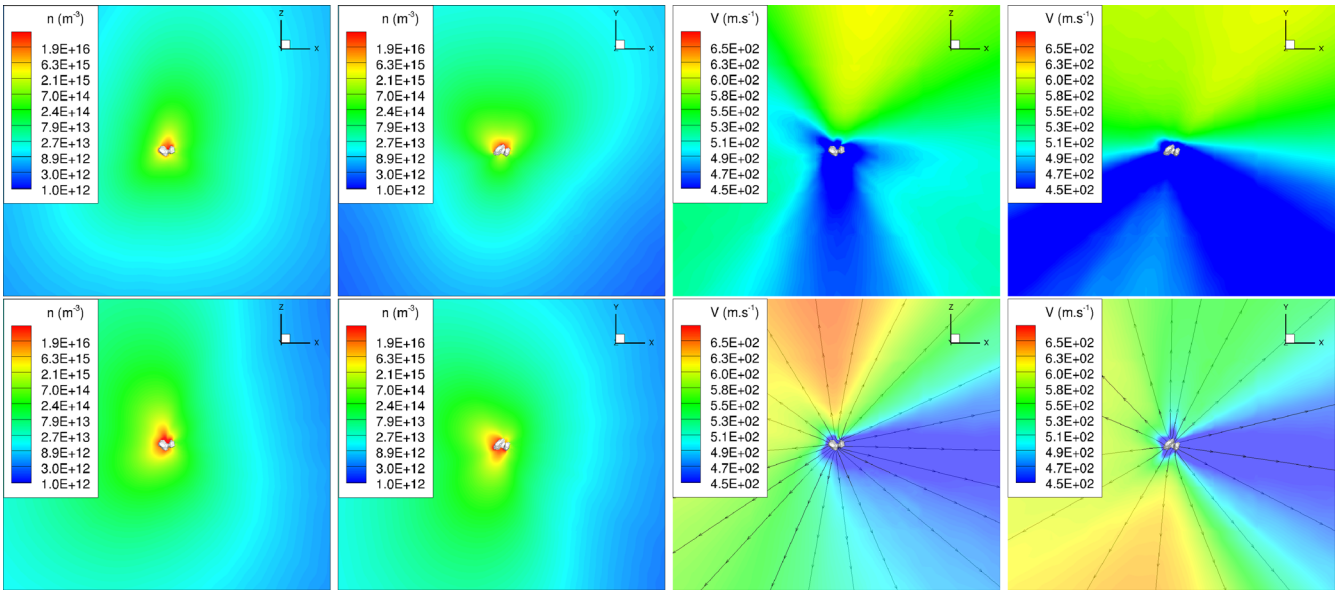

Figure 5. DSMC gas solution for H_2O showing density distribution in m^{-3} and speed in m s^{-1} in planar sections $Y = 0$ and $Z = 0$ for the case of 2015 February 24 at 00:00 UT (top panels) and for the case of 2015 March 16 at 00:00 UT (bottom panels). Each panel represents a square of 30 × 30 km. In the last two speed plots (bottom right) we plotted the streamlines of the velocity vector (Fougere et al. 2016).

averaging. The error of the GIADA velocity measurements is not statistical (Rotundi et al. 2015).

4.1 Computation of the dust grain sizes

The GIADA GDS provides the particle geometrical cross-section by applying to the measurements specific calibration curves (Della Corte et al. 2014, 2016a). The orientation of the particle while crossing the laser curtain cannot be determined. However, if the particles are slow rotators they keep their orientation while crossing the 3-mm-thick GDS laser curtain. Ivanovski et al. (2017) showed that for similar cometary conditions the non-spherical particles are slow rotators. Here we obtained very low rotation frequencies (see Section 4.2.3). How the detected particle enters into GIADA reflects on the estimation of its size. Depending on whether we assume it enters with its maximum or minimum cross-section, we derive different possible spheroid dimensions, all compatible with the GIADA geometrical cross-sections. We consider particles having a

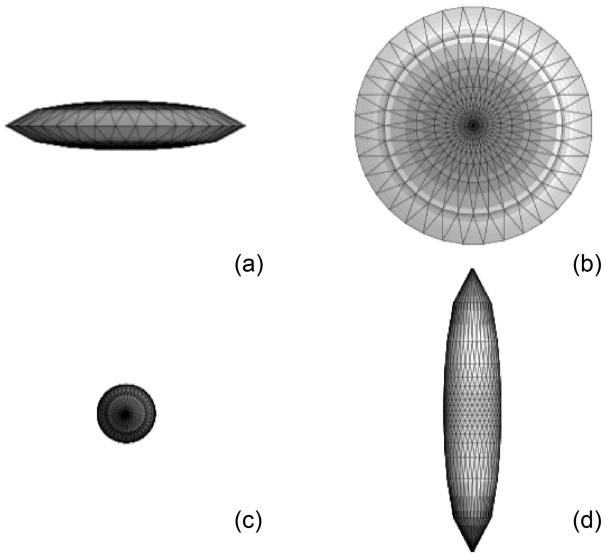

Figure 6. Minimum and maximum cross-sections of spheroidal grains: (a) is the minimum and (b) is the maximum cross-section of an oblate spheroid ($a/b = 0.2$); (c) is the minimum and (d) is the maximum cross-section of a prolate spheroid ($a/b = 5.0$).

spheroidal shape with masses (m_d) and cross-sections as measured by GIADA. We assumed homogeneous spheroids (ellipsoids of revolution) with mass m_d, semi-axis a, along the axis of revolution and semi-axis b, transverse to it. We defined four groups of dust particles depending on: (1) the spheroidal shape, i.e. prolate (Fig. 6, bottom panels) or oblate (Fig. 6, top panels), and (2) the assumed orientation they enter into GIADA, i.e. with their minimum (Figs 6a and c) or maximum (Figs 6b and d) cross-section. Starting from these four groups of particles and the particle geometrical cross-sections measured by GIADA, we derive the spheroids semi-axes and their bulk densities. For our simulations we considered the cases in agreement with GIADA data constraining the elongation and the dust bulk density (Section 4.2.1). We computed the dynamical parameters for each particle of these four groups and studied their terminal velocities and rotation frequencies (if any) in the calibrated gas outflow. Some of the studied cases are reported in five tables in the Appendix. They contain the following information:

(i) particle masses m_d measured by GIADA;
(ii) semi-axes of the spheroids, $b_{\rm obmin}$, $b_{\rm obmax}$, $b_{\rm prmin}$ and $b_{\rm prmax}$, for oblate (a/b=0.2) and prolate (a/b=5.0) spheroids;
(iii) radius of spherical particles, $b_{\rm sphere}$, identical in mass as its spheroidal equivalent;
(iv) the assumed initial orientation of the grain is 45°, and the output physical quantities are:
(v) terminal velocity of the spheroidal grain;
(vi) its rotational frequency $\nu_\infty = \omega/(2\pi)$;
(vii) the distance L_{90} at which 90 per cent of the terminal velocity has been reached and its corresponding time t_{90}. In the cases when the terminal velocity has not been achieved the reported value is the grain velocity at the distance of the GIADA detection from the comet;
(viii) the time at which the grain has started to rotate, $t_{\rm rotstart}$.

We evaluate to what extent approximating the particles detected by GIADA with spheres is realistic and we run our simulations, assuming also spherical shapes. Discarding the non-realistic dust bulk density cases, we compared the terminal velocities obtained with spheroids and spheres with the speeds measured by GIADA for individual particles.

4.2 Non-spherical computed dust velocities

To simulate particle speeds measured by GIADA, a more complex model, with respect to those based on spherical grains assumption, is needed. In fig. 1 of Fulle et al. (2016, 2017) it is shown that GIADA detected particles which would have a bulk density $>$ 10 000 kg m^{-3} if they were spheres. Only if these particles have aspect ratios up to 10 the corresponding bulk densities are $<$5000 kg m^{-3}, i.e. consistent with cometary mineralogy (e.g. Brownlee et al. 2006; Brunetto et al. 2011; Rotundi et al. 2014). Taking into account the density constraints settled by GIADA data, we simulated the motion of 30 particles detected by GIADA during P1 and P2.

The terminal velocities computed for the considered non-spherical dust particles showed differences with the GIADA measured up to 40 per cent in the case of prolate and oblate grains assumed to enter in GIADA with the minimum cross-sections (Figs 6a and c). Computed terminal velocities for two particles, assumed spheroids, with the same aspect ratio and mass, entering GIADA one with the maximum and the other one with the minimum cross-section, differ by about 60 per cent. The best agreement between the computed and measured speeds mostly occurred in the cases of oblate spheroids. The calculated terminal velocities for spheres, with the same mass and cross-section of the spheroids, turned out to be up to 90 per cent different from the GIADA measured ones (Table A5). The bias introduced by assuming a spherical shape is large and must be considered for GIADA data analysis.

4.2.1 Consistency of simulations with the GIADA data

We performed our simulations assuming spheroids of aspect ratios 5, 0.2 and 10, 0.1 used by Fulle et al. (2016, 2017), to constrain the bulk density of the complete set of particles detected by GIADA. For each GIADA detection, we performed 243 simulations combining different cases of assumed physical parameters (aspect ratio, particle orientation entering GIADA, and angle of attack) and the GIADA mass measurements.

Dealing with spheroids with aspect ratio 5 and 0.2, in Table 3 we divided GIADA detections in three groups with respect to the measured particle mass-versus-cross-section dependence (Fig. 4) and its assumed aspect ratio and orientation entering into GIADA (Fig. 6). Our simulations, when a spheroidal shape is assumed, are in agreement with GIADA data constrained in the trend mass versus cross-section for aspect ratios of 0.2 and 5 (Fig. 4). For the four detections plotted out of the constrained area, the GIADA measured speeds were not reproducible. For all remaining detections, the calculated velocity matches the trend of the GIADA speed measurements (Fig. 7). GIADA data plotting in the top left of Fig. 4, i.e. small masses and cross-sections, reproduce best the measured speeds when assuming prolate particles entering GIADA with the minimum cross-section (Fig. 6c) or oblate particles entering GIADA with the maximum cross-section (Fig. 6b). The two cases reported in Figs 6a and 6d are equivalent in terms of cross-section and the computed speeds confirm similarity also in terms of their dynamics. The GIADA data plotting in the central area of the mass-versus-cross-section plot (Fig. 4) follow the theoretical trend for spheres, and in fact for these data we find a better match between calculated and measured speeds assuming spherical particles rather than spheroids. Overall, the trend between the calculated particle speeds versus the measured masses is in agreement with the same

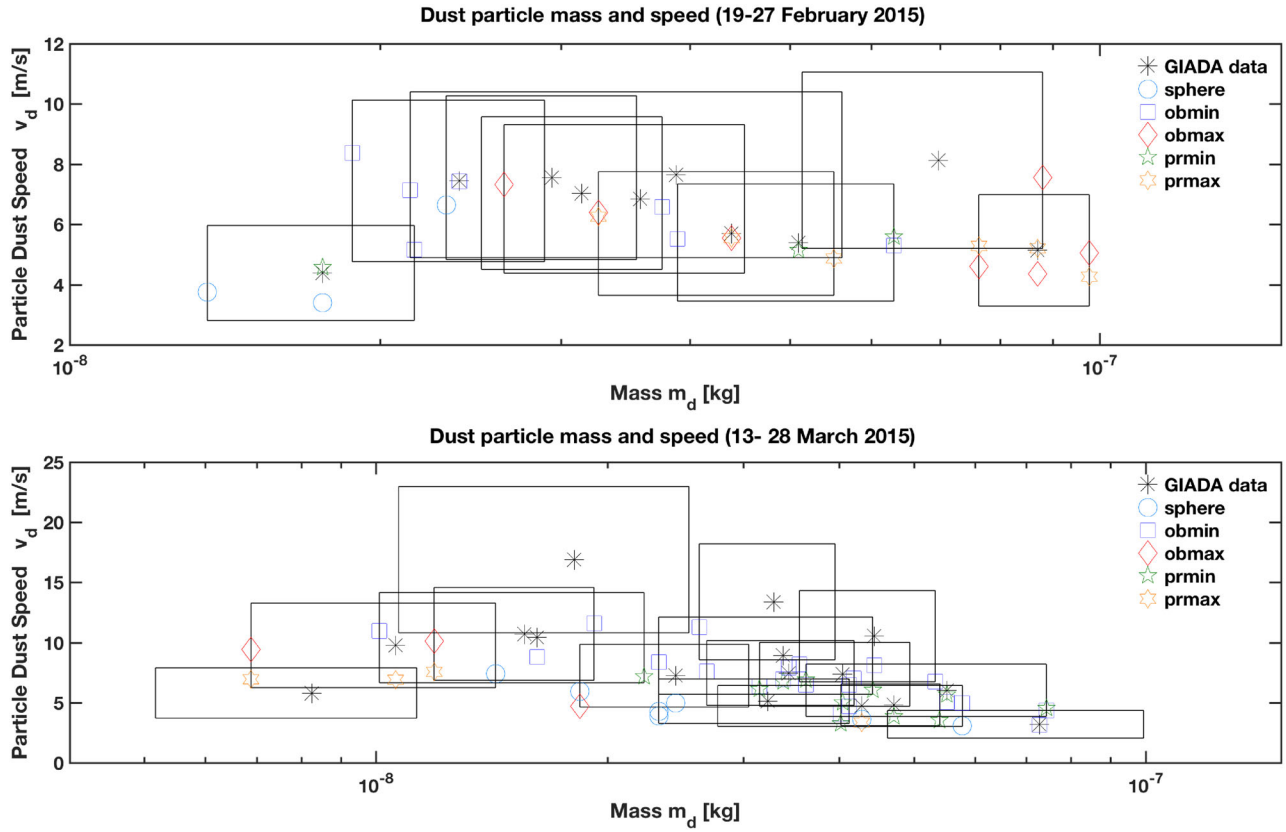

Figure 7. Computed and measured terminal velocities versus the mass measured by GIADA during P1 and P2 periods. In the cases when the terminal velocity has not been achieved, we report the dust velocity at the moment of detection. We report the computed dust particle velocities not dispersing more than 36 per cent (6 per cent being the GIADA measurement speed error plus up to 30 per cent uncertainty due to the particle initial orientation) with respect to the measured velocities measured by GIADA. The rectangles refer to GIADA measurements representing the data uncertainty due to the speed and mass errors. The simulations were performed for three mass values (measured mass, mass−error, mass + error) for each particle and for five cases combining different particle elongations and detection orientations. Each of the five cases considers: (1) spheres; (2) oblate spheroid (a/b = 0.2) entered GIADA with its minimum cross-section (*obmin*); (3) oblate spheroid (a/b = 0.2) entered GIADA with its maximum cross-section (*obmax*); (4) prolate spheroid (a/b = 5.0) entered GIADA with its minimum cross-section (*prmin*); (5) prolate spheroid (a/b = 5.0) entered GIADA with its maximum cross-section (*prmax*). The complete set of the obtained physical parameters is listed in the Appendix (Tables A1–A5).

relation found by Della Corte et al. (2016b) using only GIADA measurements.

4.2.2 *Influence of the initial grain orientation*

The initial grain orientation, i.e. the angle of attack, α, defined as the angle between the long axis of the dust grain and the local gas outflow direction (see fig. 4, Ivanovski et al. (2017)), affects the particles speed and their rotational motion. This was demonstrated by Ivanovski et al. (2017) simulating dust particles motion assuming spheroids (aspect ratio 2 and 0.5) with different initial orientation (from 0° to 90° using a step of 22.5). In the present work, we consider a single initial grain orientation of 45°, i.e. mid-case between the two limiting cases 0° and 90°. In order to evaluate the influence of the initial particle orientation in this work, we performed numerical simulations for all P1 and P2 GIADA detections with different angle of attack, i.e. from 10° to 80° with a step 10°. In Table 4 we report the results of two sets of simulation cases for two GIADA detections (cases A and B) varying the angle of attack. Changing the initial grain orientation can improve the precision of the model in reproducing the measured speed. For example, in case A the simulated grain velocity closest to the measured speed is obtained for $\alpha = 20°$. In case B, the measured speed was best reproduced for $\alpha = 80°$. The variation of the calculated speed of an individual particle with different initial orientations does not exceed 30 per cent. Since the GIADA dust speed error is 6 per cent, if we can reproduce the measured grain speeds within a range of 36 per cent, it is very likely that the initial orientation for which we obtain the GIADA speed measurement is included. These results allow us to select a single initial orientation to perform simulations for all GIADA detections, i.e. 45°, which is the mid-case between the two limiting cases 0° and 90°.

4.2.3 *Computed particle rotational frequencies*

Besides the computed terminal velocities, the model determines the rotation frequency of the simulated particles. It ranges from 0.03 to 0.2 Hz, i.e. very low particle rotational frequencies, thus compatible with our model assumptions (see Section 2.1). The simulated GIADA detected particles start rotating before they reach 90 per cent of their terminal velocities (see columns titled *t-rotstart* and *t90*, Tables A1–A4), i.e. within the acceleration region when the drag is the driving force.

Table 3. GIADA detections event day and time occurred during P1 and P2 grouped by mass-versus-cross-section dependence and its assumed orientation entering GIADA. *obmin* – oblate (a/b = 0.2) spheroid entering with its minimum cross-section; *obmax* – oblate (a/b = 0.2) spheroid entering with its maximum cross-section; *prmin* – the same as *obmin* but for prolate (a/b = 5.0) spheroid; *prmax* – the same as *obmax* but for prolate (a/b = 5.0) spheroid.

obmin (case a) and *prmax* (case d)
19/02/15 6:33 AM
20/02/15 10:57 AM
23/02/15 2:04 PM
23/02/15 4:58 PM
23/02/15 7:37 PM
26/02/15 7:50 PM
27/02/15 10:52 PM
14/03/15 7:56 PM
15/03/15 9:23 AM
15/03/15 12:27 PM
15/03/15 5:06 PM
15/03/15 9:56 PM
16/03/15 1:08 AM
16/03/15 1:37 AM
16/03/15 7:14 AM
16/03/15 12:20 PM
16/03/15 11:43 PM
18/03/15 5:22 AM
22/03/15 7:39 AM
obmax (case b)
23/02/15 4:58 PM
23/02/15 7:37 PM
24/02/15 6:31 AM
24/02/15 7:02 AM
14/03/15 10:06 AM
15/03/15 9:23 AM
16/03/15 11:43 PM
prmin (case c)
19/02/15 6:33 AM
23/02/15 2:04 PM
26/02/15 7:50 PM
27/02/15 10:52 PM
14/03/15 7:56 AM
14/03/15 7:56 PM
15/03/15 9:23 AM
15/03/15 12:27 PM

Table 4. The calculated speed of a grain at the moment of its detection for different initial orientations (α) on the nucleus surface. Case A is the event on 2015 March 18 at 5.22 AM with measured speed 7.47 m s^{-1}. The grain is assumed to be oblate ($a/b = 0.2$) and to have entered GIADA with its minimum cross-section, i.e. an *obmin* case; Case B is the event on 2015 March 15 at 12.27 PM with measured speed 6.04 m s^{-1}. The grain is assumed to be prolate ($a/b = 5.0$) and to have entered GIADA with its minimum cross-section, i.e. a *prmin* case.

Case	$\alpha(^\circ)$	v_∞(m s^{-1})
A	10	7.40
A	20	7.48
A	30	7.61
A	45	7.91
A	50	8.02
B	10	8.24
B	20	7.83
B	30	7.09
B	40	7.03
B	45	6.92
B	50	6.82
B	60	6.65
B	70	6.54
B	80	6.47

5 DISCUSSION

Our results describe the dust motion of the individual dust particles detected by GIADA, fulfilling these conditions: (1) particle detection distance from the nucleus much larger than the gas dust collisional mean-free path; (2) radial gas motion; (3) non-steep gradients for the particle velocity.

Different particle shapes, with the same mass, would influence their dynamics because of the impact on their momentum of inertia. For spheres and spheroids, with the same mass, the momentum of inertia varies only with the aspect ratio. Our aim was to study the dynamics varying the moment of inertia by varying the aspect ratio. Actually, since we considered two extremes for the spheroids, i.e. prolate (aspect ratio > 1) and oblate (aspect ratio < 1), we did evaluate the impact on our dynamical simulations of different geometries: oblate spheroids, which do approximate discs, and prolate spheroids, which do approximate cylinders. To study not approximated discs and cylinders we rigorously show in the following the difference between spheroids and cylinders with the same moment of inertia. If we consider a spheroid (with a and b major and minor semi-axis) and a cylinder (with radius R and height $2h$) of the same mass and moment of inertia, the following relation for their aspect ratios holds:

$$\frac{h}{R} = \frac{\sqrt{3}}{2}\frac{a}{b}. \tag{9}$$

Thus, the difference between the spheroid and cylinder aspect ratios is of 14 per cent. The limiting spheroid aspect ratios constraining GIADA data, i.e. 10.0 and 0.1 correspond to cylinder aspect ratios of 8.7 and 0.12, respectively. In fact, the relation between the cross-sections of the two shapes are:

$$\begin{aligned} hR &= 0.72ab \\ R^2 &= 0.85b^2. \end{aligned} \tag{10}$$

Therefore, the difference in their cross-sections ranges between 15 and 28 per cent. We here note that this difference in cross-sections between spheroids and cylinders is included in our results. In fact, the error on GIADA measurement cross-sections is of about 30 per cent and since we did simulate the entire cross-sections range, i.e. measurements with their errors, we included also the cross-sections of cylinders equivalent to the selected spheroids. In this frame, the parameters left that could bring possible differences in cylinders versus spheroids dynamic are the aerodynamic coefficients. Even if we did not consider the differences in aerodynamic coefficients for spheroids and cylinders, as their evaluation is out of

the scope of this paper, we can say that cylinders may have smaller velocities with respect to spheroids because of a less exposed cross-section to the gas flow.

The simulations we performed assuming spheroids crossing the GIADA laser curtain with the maximum cross-section suggest that aspect ratios of 5 or 10 (0.1 or 0.2) are comparable in terms of computed terminal velocities. In fact, for *prmax* and *obmax* with aspect ratios 10: 0.1, the computed terminal velocities differ less than 5 per cent with respect those computed for aspect ratios of 5: 0.2. When a particle reaches its terminal velocity in a radial and homogeneous flow likely has the maximum cross-section aligned with the direction of the gas flow. Thus, it is highly probable that the detected particles entered GIADA in this configuration. Because of the GDS subsystem geometry, i.e. detecting at 90° the signal of the crossing particle, most probably it measured the maximum particle cross-section. In this case the model does not disentangle the two particle aspect ratios because the computed velocities differ only by 5 per cent, i.e. less than the GIADA measurements speed error. On the contrary, particle velocities computed for *prmin*, *obmin* with the two sets of aspect ratio differ by 40 to 60 per cent. In this second case of particle laser crossing configuration the model can determine the particle aspect ratio that best reproduces the measured speeds.

The particle non-sphericity in our simulations permits to constrain the particle physical properties, i.e. shape (spheres or spheroids), elongation, and density, by comparing the computed terminal velocity and the GIADA measure speeds. Particle density constrain is obtained by comparing particles of the same elongation and mass assumed to enter GIADA with different cross-sections (see Tables A1–A5). With our study, we also learned more about the dynamical properties of the particles detected by GIADA, e.g. particle rotation, time and distance to achieve terminal velocity, particle initial orientation and particle orientation when entering GIADA. The particle characterization in terms of physical and dynamical properties with a feedback process allowed us to calibrate our non-spherical dust dynamical model. We plan to perform in the future more realistic dust dynamical simulations using full 3D+t gas coma solutions in order to reproduce the global dust distribution observed by GIADA.

6 CONCLUSIONS

For the first time the non-spherical dust model is used to analyse and complement *in situ* dust particle dynamical measurements performed by GIADA. The simulations provided information complementary to the GIADA measurements. More precisely, the model:

(i) refined the plausible particle elongations constrained by the trend of the mass-versus-cross-section GIADA measurements;

(ii) allowed us to identify particle rotation and to compute the rotation frequency that resulted in range from 0.03 Hz to 0.2 Hz;

(iii) checked the bias that the spherical approximation could introduce in the GIADA data analysis;

(iv) determined the most probable orientation of the particle entering GIADA.

67P/C-G dust particle terminal velocities computed with non-spherical dust model show a good agreement with speeds measured by GIADA for particles detected during P1 (2015 February 19–27) and P2 (2015 March 13–28). We reproduced particle speeds measured by GIADA with spheroids of aspect ratio 0.2 and 5 rather than spheres. We confirmed that spherical particles with bulk density consistent with cometary mineralogy cannot reproduce the particle speeds measured by GIADA.

ACKNOWLEDGEMENTS

We thank Vladimir Zakharov for critical reviews and discussions on the drafts of the manuscript.

GIADA (Grain Impact Analyser and Dust Accumulator) on-board Rosetta measures the number, mass, momentum, and velocity distribution of dust grains emitted from the cometary nucleus. GIADA was built by a consortium led by the Univ. Napoli Parthenope & INAF-Oss. Astr. Capodimonte, in collaboration with the Inst. de Astrofisica de Andalucia, Selex-ES, FI, and SENER. GIADA is presently managed & operated by Ist. di Astrofisica e Planetologia Spaziali-INAF, IT. GIADA was funded and managed by the Agenzia Spaziale Italiana, IT, with the support of the Spanish Ministry of Education and Science MEC, ES. GIADA was developed from a PI proposal from the University of Kent; sci. & tech. contribution were provided by CISAS, IT, Lab. d'Astr. Spat., FR, and Institutions from UK, Italy, France, Germany and USA. We thank the RSGS/ESAC, RMOC/ESOC & Rosetta Project/ESTEC for their outstanding work. Science support provided by NASA through the US Rosetta Project managed by the Jet Propulsion Laboratory/California Institute of Technology. GIADA calibrated data will be available through ESA's PSA web site (http://www.rssd.esa.int/index.php?project=PSA&page=index).
This research was supported by the Italian Space Agency (ASI) within the ASI-INAF agreements I/032/05/0 and I/024/12/0. Rosetta is an ESA mission with contributions from its member states and NASA. Rosetta's Philae lander is provided by a consortium led by DLR, MPS, CNES, and ASI.

Most of the computations were performed on HPC facility at the Institute of Information and Communication Technologies of the Bulgarian Academy of Sciences (IICT-BAS).

Additional computational resources used in this research have been partly supplied by INAF-IAPS through the DataWell project.

Part of this work has been accomplished at the International ISSI Team 309.

REFERENCES

Balsiger H. et al., 2007, Space Sci. Rev., 128, 745
Brownlee D. et al., 2006, Science, 314, 1711
Brunetto R. et al., 2011, Icarus, 212, 896
Capaccioni F. et al., 2015, Science, 347, aaa0628
Colangeli L. et al., 2007, Adv. Space Res., 39, 446
Combi M. R., Harris W. M., Smyth W. H., 2004, Gas Dynamics and Kinetics in the Cometary Coma: Theory and Observations. Univ. Arizona Press, Tucson, p. 523
Coradini A. et al., 2007, Space Sci. Rev., 128, 529
Crifo J. F., Rodionov A. V., 1999, Planet. Space Sci., 47, 797
Crifo J. F., Lukianov G. A., Rodionov A. V., Khanlarov G. O., Zakharov V. V., 2002, Icarus, 156, 249
Della Corte V. et al., 2014, J. Astron. Instrum., 3, 1350011
Della Corte V. et al., 2015, A&A, 583, A13
Della Corte V. et al., 2016a, Acta Astronaut., 126, 205
Della Corte V. et al., 2016b, MNRAS, 462, S210
Epifani E. et al., 2002, Adv. Space Res., 29, 1165
Esposito F., Colangeli L., Della Corte V., Palumbo P., 2002, Adv. Space Res., 29, 1159
Ferrari M., Della Corte V., Rotundi A., Rietmeijer F. J. M., 2014, Planet. Space Sci., 101, 53
Fink U. et al., 2016, Icarus, 277, 78
Fougere N., 2014, PhD thesis, University of Michigan

Fougere N. et al., 2016, A&A, 588, A134
Fulle M. et al., 2015, A&A, 583, A14
Fulle M. et al., 2016, MNRAS, 462, S132
Fulle M. et al., 2017, MNRAS, 469, S45
Gombosi T. I., 1994, Gaskinetic Theory. Cambridge Univ., Cambridge
Ivanovski S. L., Zakharov V. V., Della Corte V., Crifo J.-F., Rotundi A., Fulle M., 2017, Icarus, 282, 333
Keller H. U. et al., 2007, Space Sci. Rev., 128, 433
Landau L. D., Lifshitz E. M., 1969, Mechanics. Pergamon Press
Langevin Y. et al., 2016, Icarus, 271, 76
Palomba E., Colangeli E. L., Palumbo P., Rotundi A., Perrin J. M., Bussoletti E., 2002, Adv. Space Res., 29, 1155
Pätzold M. et al., 2016, Nature, 530, 63
Preusker F. et al., 2015, A&A, 583, A33
Rotundi A., Brucato J. R., Colangeli L., Ferrini G., Mennella V., Palomba E., Palumbo P., 2002, Meteoritics Planet. Sci., 37, 1623
Rotundi A. et al., 2014, Meteoritics Planet. Sci., 49, 550
Rotundi A. et al., 2015, Science, 347, aaa3905
Shen C., 2006, Rarefied Gas Dynamics: Fundamentals, Simulations and Micro Flows. Heat and Mass Transfer. Springer, Berlin, Heidelberg
Sierks H. et al., 2015, Science, 347, aaa1044
Tenishev V., Combi M., Davidsson B., 2008, ApJ, 685, 659
Tenishev V., Combi M. R., Rubin M., 2011, ApJ, 732, 104
Zakharov V. V., Rodionov A. V., Lukianov G. A., Crifo J. F., 2009, Icarus, 201, 358

APPENDIX A: TABLES OF NUMERICAL SIMULATIONS OF NON-SPHERICAL AND SPHERICAL PARTICLES USING THE GIADA MEASUREMENTS.

Table A1. The input parameters for the simulations are: the GIADA measured particle masses m_d [kg], the particle size derived from GIADA cross-section measurements assuming that the particles are oblate spheroids with $a/b = 0.2$ that entered GIADA with their minimum cross-section, $b_{\rm obmin}$, the initial orientation of the grain, 45°. The output parameters are: particle density, ρ_d, terminal velocity, v_∞, rotational frequency, $\nu_\infty = \omega/(2\pi)$, the distance and time at which 90 per cent of the terminal velocity has been reached, L_{90} and t_{90}, respectively, the time at which the particle has started to rotate, $t_{\rm rotstart}$.

Case	m_d [kg]	$b_{\rm obmin}$ [m]	ρ_d [kg m^{-3}]	v_∞ [m s^{-1}]	ν_∞ [Hz]	L_{90} [m]	t_{90} [s]	$t_{\rm rotstart}$ [s]
1	1.36E-08	2.32E-04	1305	8.57	0.16	79 129	10 500	1040
2	1.88E-08	2.81E-04	1016	8.38	0.15	55 745	7348	992
3	2.14E-08	2.59E-04	1469	7.14	0.14	42 103	6400	1113
4	3.89E-08	3.00E-04	1718	5.52	0.11	14 200	2670	1298
5	4.02E-08	2.25E-04	4228	4.08	0.09	15 026	3836	1830
6	2.33E-08	2.80E-04	1264	8.39	0.14	77 855	10 540	1058
7	1.01E-08	2.45E-04	815	10.97	0.2	71 720	7365	800
8	3.62E-08	3.07E-04	1492	6.5	0.12	42 315	7060	1225
9	3.55E-08	3.81E-04	767	8.19	0.13	41 715	5520	974
10	2.63E-08	3.35E-04	839	11.27	0.15	158 391	17 160	940
11	3.15E-08	2.89E-04	1550	6.36	0.12	69 637	11 327	1250
12	2.69E-08	3.35E-04	859	7.62	0.14	34 223	4814	1019

Table A2. The same as Table A1 but the size of the spheroid is $b_{\rm obmax}$, an oblate spheroid with $a/b = 0.2$ that is assumed to have entered GIADA with its maximum cross-section.

Case	m_d [kg]	$b_{\rm obmax}$ [m]	ρ_d [kg m^{-3}]	v_∞ [m s^{-1}]	ν_∞ [Hz]	L_{90} [m]	t_{90} [s]	$t_{\rm rotstart}$ [s]
1	2.32E-08	2.03E-04	3292	4.98	0.12	21 410	4517	1480
2	3.26E-08	2.86E-04	1670	6.4	0.12	55 038	9518	1300
3	2.64E-08	3.24E-04	926	7.32	0.14	30 862	4400	1064
4	7.63E-08	3.76E-04	1711	4.61	0.08	8714	1900	1480
5	4.62E-08	4.04E-04	839	7.4	0.12	39 515	5765	1070
6	6.88E-09	1.65E-04	1817	9.43	0.2	92 808	11 360	975
7	1.84E-08	1.75E-04	4080	4.7	0.12	10 796	2371	1595
8	1.19E-08	1.86E-04	2194	10.11	0.17	193 983	24 000	1115

Table A3. The input parameters for the simulations are: the GIADA measured particle masses m_d [kg], the particle size derived from GIADA cross-section measurements assuming that the particles are prolate spheroids with a/b= 5.0 that entered GIADA with their minimum cross-section, $b_{\rm prmin}$, the initial orientation of the grain, 45°. The output parameters are: particle density, ρ_d, terminal velocity, v_∞, rotational frequency, $\nu_\infty = \omega/(2\pi)$, the distance and time at which 90 per cent of the terminal velocity has been reached, L_{90} and t_{90}, respectively, the time at which the particle has started to rotate, $t_{\rm rotstart}$.

Case	m_d [kg]	$b_{\rm prmin}$ [m]	ρ_d [kg m^{-3}]	v_∞ [m s^{-1}]	ν_∞ [Hz]	L_{90} [m]	t_{90} [s]	$t_{\rm rotstart}$ [s]
1	3.89E-08	1.34E-04	768	7.15	0.06	110 018	18 040	1395
2	1.19E-07	1.16E-04	3672	2.6	0.03	23 560	9524	2980
3	4.02E-08	1.00E-04	1891	3.28	–	4203	1058	–
4	3.62E-08	1.37E-04	667	6.92	0.06	70 822	11 500	1308
5	3.15E-08	1.29E-04	693	6.14	0.06	43 735	7396	1335

Table A4. The same as Table A3 but the size of the spheroid, $b_{\rm prmax}$, i.e. a prolate spheroid with a/b= 5.0 that is assumed to have entered GIADA with its maximum cross-section.

Case	m_d [kg]	$b_{\rm prmax}$ [m]	ρ_d [kg m^{-3}]	v_∞ [m s^{-1}]	ν_∞ [Hz]	L_{90} [m]	t_{90} [s]	$t_{\rm rotstart}$ [s]
1	2.32E-08	9.09E-05	1472	5.46	0.06	57 024	11 550	1590
2	3.26E-08	1.28E-04	747	6.26	0.06	58 009	10 260	1400
3	7.63E-08	1.68E-04	765	5.28	0.04	64 536	13 660	1690
4	1.01E-08	4.90E-05	4077	3.75	0.07	8972	2405	1935
5	3.55E-08	7.62E-05	3836	3.82	0.05	69 821	20 600	2365
6	2.63E-08	6.69E-05	4196	3.95	0.05	69 150	19 700	2290
7	1.07E-08	6.96E-05	1514	6.19	0.08	53 172	9450	1390
8	6.88E-09	7.39E-05	813	6.94	0.1	9597	1400	1055
9	1.84E-08	7.84E-05	1824	4.57	0.06	9661	2160	1690
10	1.19E-08	8.33E-05	981	7.55	0.08	76 061	11 400	1220
11	2.69E-08	6.69E-05	4297	3.83	0.05	88 761	26 700	2495
12	2.78E-08	8.50E-05	2167	1.99	0.03	18 893	9910	3830

Table A5. The input parameters for the simulations are: the GIADA measured particle masses m_d [kg], the particle size derived from GIADA cross-section measurements assuming that the particles are spheres, $b_{\rm sphere}$. The output parameters are: particle density, ρ_d, terminal velocity, v_∞, the distance and time at which 90 per cent of the terminal velocity has been reached, L_{90} and t_{90}, respectively.

Case	m_d [kg]	$b_{\rm sphere}$ [m]	ρ_d [kg m^{-3}]	v_∞ [m s^{-1}]	L_{90} [m]	t_{90} [s]
1	1.36E-08	1.04E-04	2919	3.75	22 055	6348
2	2.51E-08	1.76E-04	1103	6.02	109 282	21 785
3	1.88E-08	1.26E-04	2272	4.47	63 080	16 100
4	2.32E-08	2.03E-04	658	6.65	56 868	9650
5	2.14E-08	1.16E-04	3284	3.55	31 563	9702
6	3.89E-08	1.34E-04	3841	2.9	23 330	8677
7	2.33E-08	1.25E-04	2827	3.88	40 637	11 585
8	1.01E-08	1.10E-04	1823	5.76	71 624	14 310
9	3.55E-08	1.70E-04	1715	3.82	17 113	4790
10	2.63E-08	1.50E-04	1876	4.82	69 873	16 630
11	1.07E-08	1.56E-04	677	7.88	69 266	10 080
12	2.67E-09	8.19E-05	1161	6.92	21 877	3397
13	2.29E-09	8.72E-05	826	9.45	69 645	8441
14	3.15E-08	1.29E-04	3465	3.12	21 883	7491
15	1.84E-08	1.75E-04	816	5.94	70 694	12 390
16	2.69E-08	1.50E-04	1922	4.19	51 752	13 880
17	2.33E-08	1.67E-04	1185	4.27	58 450	14 293

This paper has been typeset from a TEX/LATEX file prepared by the author.